Acta Polytechnica **61**(SI):59–67, 2021
DOI:10.14311/AP.2021.61.0059

available online at https://ojs.cvut.cz/ojs/index.php/ap

NUMERICAL SIMULATION OF A SINGLE RING INFILTRATION EXPERIMENT WITH *hp*-ADAPTIVE SPACE-TIME DISCONTINUOUS GALERKIN METHOD

Vít Dolejší[b], Michal Kuráž[c], Pavel Solin[a,*]

[a] *University of Nevada, College of Science, Department of Mathematics and Statistics, 1664 N Virginia St, NV 89557 Reno, USA*

[b] *Charles University, Faculty of Mathematics and Physics, Sokolovská 83, 186 75 Prague, Czech Republic*

[c] *Czech University of Life Sciences Prague, Faculty of Environmental Sciences, Department of Water Resources and Environmental Modeling, Kamýcká 129, 165 00 Prague, Czech Republic*

[*] corresponding author: solin@unr.edu

Abstract. We present a novel *hp*-adaptive space-time discontinuous Galerkin (*hp*-STDG) method for the numerical solution of the nonstationary Richards equation equipped with Dirichlet, Neumann and seepage face boundary conditions. The *hp*-STDG method presented in this paper is a generalization of a *hp*-STDG method which was developed for time dependent non-linear convective-diffusive problems. We describe the method and the single ring experiment, and then we present a numerical experiment which clearly demonstrates the superiority of the *hp*-STDG method over a discontinuous Galerkin method based on a static fine mesh.

Keywords: Richards equation, porous media flow, space-time discontinuous Galerkin method.

1. Introduction

The single ring (hereafter SR) infiltration experiment is a standard and robust dynamic field experiment. The steady part of this experiment is traditionally used for the identification of saturated hydraulic conductivity. More recently, the unsteady part of this experiment was used to analyze various hydraulic properties of soils such as van Genuchten's α (see, for example, [1] and [2]).

The SR experiment can be mathematically described by the *Richards equation* [3], which is a governing equation for many different applications ranging from hydrology, soil and snow physics [4–6], contaminant transport simulations [7], etc.

The Richards equation belongs to the class of *quasi-linear degenerate parabolic equations* since the space and time derivative terms can vanish or blow up. The analytical results concerning the existence and uniqueness were published, e.g., in [8–10]. First attempts of solving the Richards equation numerically date back to [11] in the 1970s. Various methods for the numerical solution of the Richards equation have been studied and improved in the last decades [12–20].

There are two main reasons why *hp*-adaptive discontinuous Galerkin methods are naturally suitable for the numerical simulation of the SR experiment:

(1.) The flow pattern is typically formed out of a moving wetting front. This wetting front is the source of considerable computational difficulties due to steep gradients in the solution and abrupt changes in nonlinear functions.

(2.) The flow domain is effectively discontinuous, since the thickness of the steel ring ($\approx$ 1 mm) is negligible compared to the scale of the flow pattern, as shown in Fig. 1.

In this paper we use the discontinuous Galerkin (DG) method to solve the nonstationary Richards equation describing the SR experiment. The Richards equation is equipped with both Dirichlet and Neumann boundary conditions (BCs), as well as with a seepage face boundary condition (BC). We combine the DG method with an anisotropic mesh adaptation algorithm and present a simulation of the SR experiment which demonstrates the full potential of the proposed numerical treatment for this class of problems.

2. Governing equations

We will model the single ring infiltration experiment using the nonstationary planar Richards equation in the form

$$C(\psi)\frac{\partial \Psi}{\partial t} - \nabla \cdot (\mathbf{K}(\psi)\nabla \Psi) = 0, \qquad (2.1)$$

where ψ denotes the pressure head [L] and Ψ is the hydraulic head [L]. They are connected by the simple relation

$$\Psi = \psi + z, \qquad (2.2)$$

where z is the vertical distance from the reference level (the geodetic head [L]). Moreover, the tensor function $\mathbf{K}(\psi)$ is the unsaturated hydraulic conductivity [L.T^{-1}], and it is defined as the product

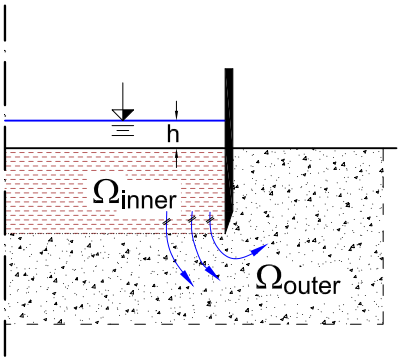

Figure 1. Scheme of the single ring infiltration experiment.

of the the relative hydraulic conductivity $K_r(\psi)$ [-] and the (tensor value) saturated hydraulic conductivity $\mathbf{K}_s$ [L.T^{-1}],

$$\mathbf{K}(\psi) = K_r(\psi)\mathbf{K}_s. \tag{2.3}$$

Furthermore, the scalar function $C(\psi)$ denotes the water retention capacity [L^{-1}], expressed in the form

$$C(\psi) = \frac{\mathrm{d}\theta(\psi)}{\mathrm{d}\psi} + \frac{\theta(\psi)}{\theta_S} S_s, \tag{2.4}$$

where the symbol $\theta(\psi)$ denotes the water content function [-], and θ_S is the limited saturated water content [-] and S_s is the specific storativity (aquifer storage) [L^{-1}].

The function $\theta(\psi)$ is given by the van Genuchten's law [21], which can be written in the form

$$\theta(\psi) = \begin{cases} \dfrac{\theta_s - \theta_r}{(1 + (-\alpha\psi)^n)^m} + \theta_r, & \text{for } \psi < 0, \\ \theta_s & \text{for } \psi \geq 0, \end{cases} \tag{2.5}$$

where θ_r[-] is the residual water content, θ_s[-] is the saturated water content, n [-] and m [-] are pore size distribution parameters, and α [L^{-1}] is given as the inverse of the air entry value.

The relative conductivity $K_r(\psi)$ appearing in (2.3) is given by the Mualem function [22] which in combination with (2.5) reads

$$K_r(\psi) = \begin{cases} \dfrac{\left(1-(-\alpha\psi)^{m\,n}(1+(-\alpha\psi)^n)^{-m}\right)^2}{(1+(-\alpha\psi)^n)^{m/2}} & \text{for } \psi < 0, \\ 1 & \text{for } \psi \geq 0, \end{cases} \tag{2.6}$$

In order to close the Richard's equation (2.1) we add the usual Dirichlet and Neumann BCs. Moreover, in order to simulate the seepage of the fluid from the medium through its boundary, we consider also the *seepage face boundary condition* which reads

$$\psi := \Psi - z \leq 0, \quad -\mathbf{K}(\Psi - z)\nabla\Psi \cdot \boldsymbol{n} \geq 0, \quad \psi(\nabla\Psi \cdot \boldsymbol{n}) = 0. \tag{2.7}$$

The first condition in (2.7) means that the pressure head ψ must be non-positive and the second one means that the fluid cannot flow into the medium because there is no fluid outside the medium. Finally, the last relation in (2.7) gives that the fluid leaves the medium if and only if the medium becomes saturated ($\psi = 0$).

For the purpose of numerical implementation we have to reformulate (2.7). According to [23], we treat the seepage BC as a Signorini condition. This means that if the medium on the boundary is unsaturated ($\psi < 0$) then this boundary behaves as a no-flow (homogeneous Neumann) boundary. On the other hand, if the medium on the boundary is saturated then the boundary changes into a Dirichlet one with a zero pressure head. These conditions can be then written as

$$\nabla\Psi \cdot \boldsymbol{n} = 0, \quad \text{if} \quad \psi < 0, \tag{2.8a}$$

$$\psi = 0, \quad \text{if} \quad \nabla\Psi \cdot \boldsymbol{n} < 0. \tag{2.8b}$$

2.1. Initial boundary value problem

In order to formulate (2.1) in a form more suitable for numerical discretization, and taking into account (2.2), we write the first term in (2.1) as

$$C(\psi)\frac{\partial\Psi}{\partial t} = C(\Psi - z)\frac{\partial\Psi}{\partial t} = C(\Psi - z)\frac{\partial(\Psi - z)}{\partial t} = \frac{\partial\vartheta(\Psi - z)}{\partial t} = \frac{\partial\vartheta(\psi)}{\partial t}. \tag{2.9}$$

Here, in virtue of (2.4), we define the quantity

$$\vartheta(\psi) := \theta(\psi) + \frac{S_s}{\theta_S}\int_{-\infty}^{\psi} \theta(s)\mathrm{d}s \tag{2.10}$$

which represents the *active pore volume* affected by the changing pressure (hydrostatic and capillary). For vanishing specific storage S_s, the active pore volume $\vartheta(\psi)$ coincides with the water content $\theta(\psi)$.

Now we are ready to formulate the initial boundary value problem. The porous medium occupies a domain $\Omega \subset \mathbb{R}^2$. If $x \in \Omega$ then we write either $x = (x_1, x_2)$ or $x = (x_1, z)$. Furthermore, the symbol Γ denotes the boundary of Ω, $T > 0$ is the final physical time of our interest and we put $I := (0, T)$. Moreover, symbols

Γ_D, Γ_N and Γ_E, respectively, denotes the corresponding parts of Γ, where the Dirichlet, Neumann and seepage face BCs are prescribed, respectively. Obviously, these parts have to be mutually disjoint and $\Gamma_D \cup \Gamma_N \cup \Gamma_E = \Gamma$.

In virtue of (2.1) and (2.8) – (2.9), we define the following problem. Find a function $\Psi = \Psi(x,t) : \Omega \times I \to \mathbb{R}$ such that

$$\frac{\partial \vartheta(\psi)}{\partial t} - \nabla \cdot (\mathbf{K}(\psi)\nabla\Psi) = 0 \quad \text{in } \Omega \times I, \tag{2.11a}$$

$$\Psi = \Psi_D \quad \text{on } \Gamma_D \times I, \tag{2.11b}$$

$$\mathbf{K}(\psi)\nabla\Psi \cdot \boldsymbol{n} = \boldsymbol{q}_N \quad \text{on } \Gamma_N \times I, \tag{2.11c}$$

$$\left.\begin{aligned} \nabla\Psi \cdot \boldsymbol{n} = 0 \text{ if } \Psi \le 0 \\ \Psi = 0 \text{ if } \nabla\Psi \cdot \boldsymbol{n} \le 0 \end{aligned}\right\} \quad \text{on } \Gamma_E \times I, \tag{2.11d}$$

$$\Psi(x, t=0) = \Psi_0 \quad \text{in } \Omega. \tag{2.11e}$$

3. Space-time discontinuous Galerkin discretization

We solve (2.11) numerically using the *space-time discontinuous Galerkin (STDG)* method. We refer to [24] where it was developed for the numerical solution of a time-dependent partial differential equation. Here, we present its adaptation for the Richards equation.

3.1. Space-time partition

First, using a finite sequence $0 = t_0 < t_1 < \ldots < t_r = T$ we split the time interval I into sub-intervals intervals $I_m = (t_{m-1}, t_m],\ m = 1, \ldots, r$ of lengths $|I_m| = \tau_m$. We define $\tau = \max_{m=1,\ldots,r}\tau_m$. For each interval $t_m,\ m = 1, \ldots, r$, we consider a triangulation $\mathscr{T}_{h,m}$ of Ω consisting of a finite number of closed mutually disjoint triangles K covering $\overline{\Omega}$, i.e., $\overline{\Omega} = \cup_{K\in\mathscr{T}_{h,m}} K,\ m = 0, \ldots, r$. The meshes $\mathscr{T}_{h,m}$ can differ for each time level. By ∂K and h_K we denote the boundary and the diameter, respectively, of $K \in \mathscr{T}_{h,m}$.

Furthermore, by $\Gamma_{h,m}$ we denote the set of edges of $\mathscr{T}_{h,m}$. We define several subsets of $\Gamma_{h,m}$, namely

$$\begin{aligned}
\Gamma^I_{h,m} &= \{\gamma \in \Gamma_{h,m},\ \gamma \subset \Omega\} \quad \text{(interior edges)}, \\
\Gamma^D_{h,m} &= \{\gamma \in \Gamma_{h,m},\ \gamma \subset \Gamma_D\} \quad \text{(Dirichlet edges)}, \\
\Gamma^N_{h,m} &= \{\gamma \in \Gamma_{h,m},\ \gamma \subset \Gamma_N\} \quad \text{(Neumann edges)}, \\
\Gamma^E_{h,m} &= \{\gamma \in \Gamma_{h,m},\ \gamma \subset \Gamma_E\} \quad \text{(seepage face edges)}, \\
\Gamma^B_{h,m} &= \Gamma^D_{h,m} \cup \Gamma^N_{h,m} \cup \Gamma^E_{h,m}, \\
\Gamma^{ID}_{h,m} &= \Gamma^I_{h,m} \cup \Gamma^D_{h,m}.
\end{aligned} \tag{3.1}$$

Finally, a unit normal to $\gamma \in \Gamma_{h,m}$ is denoted by $\boldsymbol{n}_\gamma$. We assume that vectors $\boldsymbol{n}_\gamma$, $\gamma \in \Gamma^B_{h,m}$ are outer normals to $\partial\Omega$. The orientation of $\boldsymbol{n}_\gamma$ of interior edges $\gamma \in \Gamma^I_{h,m}$ is arbitrary but fixed.

3.2. Finite element space

We will seek the approximate solution in a space of *piecewise polynomial* but *discontinuous functions*. We use a fixed polynomial degree $q \in \mathbb{N}$ wrt. $t \in I$ but a possibly varying polynomial degree p_K wrt. $x \in \Omega$ for each mesh element $K \in \mathscr{T}_{h,m}$, $m = 0, \ldots, r$. We define the spaces of space-time discontinuous piecewise polynomial functions on $\Omega \times I$ as

$$\begin{aligned} S^{\tau,q}_{h,p} := \{\varphi : \Omega \times I \to \mathbb{R};\ \varphi|_{K\times I_m} \in P^{p_K,q}(K \times I_m), \\ K \in \mathscr{T}_{h,m},\ m = 1, \ldots, r\}, \end{aligned} \tag{3.2}$$

where $P^{p_K,q}(K \times I_m)$ is the space of space-time polynomial functions on $K \times I_m$ having degree $\le p_K$ wrt. $x \in K$ and degree $\le q$ wrt. $t \in I_m$ for $K \in \mathscr{T}_{h,m}$ and $m = 1, \ldots, r$.

Moreover, a restriction of $S^{\tau,q}_{h,p}$ on the time layer I_m, $m = 1, \ldots, r$ is given by

$$\begin{aligned} S^{\tau,q}_{m,h,p} := \{\varphi : \Omega \times I_m \to \mathbb{R}; \\ \varphi|_{K\times I_m} \in P^{p_K,q}(K \times I_m),\ K \in \mathscr{T}_{h,m}\}. \end{aligned} \tag{3.3}$$

Finally, we introduce the jumps and mean values of functions from $S^{\tau,q}_{h,p}$. For $\gamma \in \Gamma^I_{h,m}$ and $v \in S^{\tau,q}_{m,h,p},\ m = 0, \ldots, r$ we define

$$[v]_\gamma = v|^{(+)}_\gamma - v|^{(-)}_\gamma, \tag{3.4}$$

$$\langle v \rangle_\gamma = \tfrac{1}{2}\big(v|^{(+)}_\gamma + v|^{(-)}_\gamma\big), \tag{3.5}$$

where $v|^{(\pm)}_\gamma = \lim_{\delta\to 0\pm} v(x + \delta\boldsymbol{n}_\gamma)$, $x \in \gamma$. For $\gamma \in \Gamma^B_{h,m}$, we set $[v]_\gamma = \langle v \rangle_\gamma = v|_\gamma$. In the case that $\boldsymbol{n}_\gamma$, $[\cdot]_\gamma$ and $\langle\cdot\rangle_\gamma$ are arguments of $\int_\gamma \ldots \mathrm{d}S$, $\gamma \in \Gamma_{h,m}$ we omit the subscript γ.

Additionally, we set

$$\{\varphi\}_m := \varphi|^+_m - \varphi|^-_m, \quad \varphi|^\pm_m := \lim_{\delta\to 0\pm} \varphi(t_m + \delta), \tag{3.6}$$

defining a jump of $\varphi \in S^{\tau,q}_{h,p}$ wrt. time at $t_m,\ m = 0, \ldots, r$.

We observe that the finite element space $S^{\tau,q}_{h,p}$ is independent on the type of boundary conditions since they are incorporated directly in the numerical scheme. This is different from conforming finite element methods.

3.3. Space discretization

We discretize problem (2.11) in space using the *incomplete interior penalty Galerkin (IIPG)* method. The main advantage of the IIPG technique is the absence of additional stabilization terms, cf. [24, Chapter 2]. In order to simplify an exposition of IIPG method, we assume in this section that $\Gamma_E = \emptyset$. The general case will be discussed in Section 3.4.

Let Ψ be a sufficiently smooth exact solution of (2.11). Let $m = 1, \ldots, r$ be arbitrary but fixed. We multiply (2.11a) with $\varphi \in S^{\tau,q}_{h,p}$, integrate over $K \in \mathscr{T}_{h,m}$, sum over all elements $K \in \mathscr{T}_{h,m}$, and carry out some manipulation. The Green's theorem applied to

the conductivity term and (2.11c) yields

$$
\begin{aligned}
&- \sum_{K\in\mathscr{T}_{h,m}} \int_K \nabla\cdot(\mathbf{K}(\Psi - z)\nabla\Psi)\varphi \,\mathrm{d}x \qquad (3.7)\\
&= \sum_{K\in\mathscr{T}_{h,m}} (\mathbf{K}(\Psi - z)\nabla\Psi, \nabla\varphi)_K\\
&\quad - \sum_{\gamma\in\Gamma^{ID}_{h,m}} (\langle\mathbf{K}(\Psi - z)\nabla\Psi\rangle\cdot\boldsymbol{n}, [\varphi])_\gamma\\
&\quad - \sum_{\gamma\in\Gamma^{N}_{h,m}} (\boldsymbol{q}_N, \varphi)_\gamma.
\end{aligned}
$$

In order to ensure the coercivity of the resulting numerical scheme, we include additional terms to (3.7) which are vanishing if Ψ is smooth and satisfies (2.11b). Namely,

$$
\sum_{\gamma\in\Gamma^{I}_{h,m}} (\sigma[\Psi], [\varphi])_\gamma + \sum_{\gamma\in\Gamma^{D}_{h,m}} (\sigma(\Psi - \Psi_D), \varphi)_\gamma, \quad (3.8)
$$

where σ is the penalty parameter. The terms in (3.8) are called the *interior* and *boundary penalties* and they replace the interelement continuity of approximate solution from $S^{\tau,q}_{h,p}$.

Taking into account (3.7)–(3.8), we obtain the relation

$$
(\partial_t\vartheta(\Psi), \varphi)_\Omega + a_{h,m}(\Psi, \varphi) = 0 \quad \forall\varphi \in S^{\tau,q}_{h,p}, \quad (3.9)
$$

where

$$
\begin{aligned}
a_{h,m}(\Psi, \varphi) := &\sum_{K\in\mathscr{T}_{h,m}} (\mathbf{K}(\Psi - z)\nabla\Psi, \nabla\varphi)_K \qquad (3.10)\\
&- \sum_{\gamma\in\Gamma^{ID}_{h,m}} (\langle\mathbf{K}(\Psi - z)\nabla\Psi\rangle\cdot\boldsymbol{n}, [\varphi])_\gamma\\
&+ \sum_{\gamma\in\Gamma^{I}_{h,m}} (\sigma[\varphi], [\Psi])_\gamma\\
&+ \sum_{\gamma\in\Gamma^{D}_{h,m}} (\sigma\varphi, \Psi - \Psi_D)_\gamma - (\boldsymbol{q}_N, \varphi)_{\Gamma_N}.
\end{aligned}
$$

Let us note that Ψ and φ are functions of $x = (x_1, x_2) = (x_1, z) \in \Omega$ and $t \in I$.

3.4. Numerical realization of seepage face boundary (2.8)

In this section, we extend the IIPG discretization of (2.1) from Section 3.3 to a general case, i.e., $\Gamma_E \neq \emptyset$. Similarly as in [23], we implement condition (2.8) using the scheme

$$
\begin{aligned}
&\text{if} \quad \psi < 0 \text{ and } \nabla\Psi\cdot\boldsymbol{n} > 0 \quad \text{then} \quad \nabla\Psi\cdot\boldsymbol{n} = 0,\\
&\text{if} \quad \psi < 0 \text{ and } \nabla\Psi\cdot\boldsymbol{n} < 0 \quad \text{then} \quad \nabla\Psi\cdot\boldsymbol{n} = 0,\\
&\text{if} \quad \psi > 0 \text{ and } \nabla\Psi\cdot\boldsymbol{n} > 0 \quad \text{then} \quad \nabla\Psi\cdot\boldsymbol{n} = 0,\\
&\text{if} \quad \psi > 0 \text{ and } \nabla\Psi\cdot\boldsymbol{n} < 0 \quad \text{then} \quad \psi = 0,
\end{aligned} \qquad (3.11)
$$

The quantities before "then" are taken from the interior of Ω and the equalities after "then" correspond to the prescribed BCs.

Let us note that practical implementation of (3.11) in the framework of conforming finite element methods is quite difficult since the finite element space, where the approximate solution is sought, depends on the Dirichlet part of boundary Γ_D and then the realization of (3.11) requires frequent changes of finite element space.

The realization of (3.11) using the DG method is much easier. On the seepage face part of boundary Γ_E, we define a scalar function $\sigma^* : \Gamma_E \to \{0, 1\}$ whose role is to switch between (2.8a) (Neumann BC) for $\sigma^* = 0$ and (2.8b) (Dirichlet BC) for $\sigma^* = 1$. Then we supplement the form (3.10) by additional integrals over Γ_E in the form

$$
\begin{aligned}
a_{h,m}(\Psi, \varphi) := &\sum_{K\in\mathscr{T}_{h,m}} (\mathbf{K}(\Psi - z)\nabla\Psi, \nabla\varphi)_K \qquad (3.12)\\
&- \sum_{\gamma\in\Gamma^{ID}_{h,m}} (\langle\mathbf{K}(\Psi - z)\nabla\Psi\rangle\cdot\boldsymbol{n}, [\varphi])_\gamma\\
&- \sum_{\gamma\in\Gamma^{E}_{h,m}} (\sigma^*\mathbf{K}(\Psi - z)\nabla\Psi\cdot\boldsymbol{n}, \varphi)_\gamma\\
&+ \sum_{\gamma\in\Gamma^{I}_{h,m}} (\sigma[\varphi], [\Psi])_\gamma\\
&+ \sum_{\gamma\in\Gamma^{D}_{h,m}} (\sigma\varphi, \Psi - \Psi_D)_\gamma\\
&+ \sum_{\gamma\in\Gamma^{E}_{h,m}} (\sigma^*\sigma\varphi, \Psi - z)_\gamma - (\boldsymbol{q}_N, \varphi)_{\Gamma_N}.
\end{aligned}
$$

Form $a_{h,m}$ from (3.12) behaves in the following way: Let $g_E \subset \Gamma_E$ be an arbitrary but fixed part of the seepage face boundary. If $\sigma^*|_{g_E} = 1$ then Dirichlet BC $\Psi = z$ is enforced on g_E. On the other hand, if $\sigma^*|_{g_E} = 0$ then the homogeneous Neumann BC is used on g_E.

Now, let us discuss the choice of the function σ^* in (3.12). In virtue of (3.11), we set σ^* according to the signs of ψ and $-\mathbf{K}(\Psi - z)\nabla\Psi\cdot\boldsymbol{n}$ on Γ_E. Therefore, we define

$$
\sigma^*(\Psi(x,t)) = \begin{cases} 1 & \text{if } \psi(x,t) \geq 0 \text{ and } \nabla\Psi\cdot\boldsymbol{n} \leq 0,\\ 0 & \text{otherwise .}\end{cases} \qquad (3.13)
$$

However, this choice is not suitable from the practical point of view because the function σ^* only admits two distinct values 0 and 1. As a result, iterative solvers for the resulting algebraic system will fail to converge. This unpleasant effect can be suppressed via smoothing of σ^* near the transition from $\sigma^* = 0$ and $\sigma^* = 1$.

Hence, we introduce *transition regions* of small widths $s_{\mathrm{ph}} > 0$ and $s_{\mathrm{fl}} > 0$, and define a function $\sigma^*_h(\Psi(x,t))$ which is continuously differentiable with respect to Ψ. It is equal to σ^* if $\psi(x,t) \notin [0, s_{\mathrm{ph}}]$ and $\mathbf{K}(\Psi - z)\nabla\Psi\cdot\boldsymbol{n} \notin [0, s_{\mathrm{fl}}]$.

In order to ensure the consistency of the resulting numerical scheme, the transition regions must vanish for a vanishing mesh size. Therefore we define

$s_{\mathrm{ph}}|_K := c_1\, h_K$ and $s_{\mathrm{fl}}|_K := c_2\, h_K$, where $c_1 > 0$ and $c_2 > 0$ are empirically chosen constants. Typically we use the values $c_1 = c_2 = 0.1$. Numerical experiments show that the numerical scheme only depends weakly on $s_{\mathrm{ph}}|_K$ and $s_{\mathrm{fl}}|_K$.

Finally, we replace σ^* in (3.12) with σ_h^* and obtain

$$\begin{aligned} a_{h,m}(\Psi,\varphi) := & \sum_{K\in\mathscr{T}_{h,m}} (\mathbf{K}(\Psi - z)\nabla\Psi, \nabla\varphi)_K \\ & - \sum_{\gamma\in\Gamma_{h,m}^{ID}} (\langle \mathbf{K}(\Psi - z)\nabla\Psi\rangle\cdot\boldsymbol{n}, [\varphi])_\gamma \\ & - \sum_{\gamma\in\Gamma_{h,m}^{E}} (\sigma_h^*(\Psi)\mathbf{K}(\Psi - z)\nabla\Psi\cdot\boldsymbol{n}, \varphi)_\gamma \\ & + \sum_{\gamma\in\Gamma_{h,m}^{I}} (\sigma[\varphi], [\Psi])_\gamma \\ & + \sum_{\gamma\in\Gamma_{h,m}^{D}} (\sigma\varphi, \Psi - \Psi_D)_\gamma \\ & + \sum_{\gamma\in\Gamma_{h,m}^{E}} (\sigma_h^*(\Psi)\sigma\varphi, \Psi - z)_\gamma - (\boldsymbol{q}_N, \varphi)_{\Gamma_N}. \end{aligned} \tag{3.14}$$

3.5. Time discretization

The time discretization is carried out using the *space-time discontinuous Galerkin method* (STDGM) (see [24]), which reads

$$A_{h,m}(\Psi,\varphi) = 0 \qquad \forall\varphi\in S_{h,p}^{\tau,q},\ m = 1,\dots,r, \tag{3.15}$$

where

$$\begin{aligned} A_{h,m}(\Psi,\varphi) = & \int_{I_m} \big((\partial_t\vartheta(\Psi - z),\varphi)_\Omega + a_{h,m}(\Psi,\varphi)\big)\mathrm{d}t \\ & + (\{\vartheta(\Psi - z)\}_{m-1}, \varphi|_{m-1}^+)_\Omega. \end{aligned} \tag{3.16}$$

Now, we define the final *hp*-space-time discontinuous Galerkin (*hp*-STDG) solution of problem (2.11):

Definition 3.1. *Let $A_{h,m}$ be the form* (3.16)*. The function $\Psi_{h\tau}\in S_{h,p}^{\tau,q}$ is called the* approximate solution *of* (2.11) *if*

$$A_{h,m}(\Psi_{h\tau},\varphi) = 0 \quad \forall\varphi\in S_{h,p}^{\tau,q},\ m = 1,\dots,r \tag{3.17}$$

where $\Psi_{h\tau}|_0^- := \Psi_0$, cf. (2.11e)*.*

The term $(\{\vartheta(\Psi - z)\}_{m-1}, \varphi|_{m-1}^+)_\Omega$ in (3.16) replaces in some sense the interelement continuity in time. The approximate solutions on two subsequent time layers are connected together only by this term. A major advantage of this treatment is that different grids (and polynomial degrees p_K, $K\in\mathscr{T}_{h,m}$) can be used in each time interval separately. This is advantageous from the point of view of adaptive methods.

3.6. Solution of the discrete problem

The approximate solution (3.17) represents a sequence of r nonlinear algebraic systems of equations, one system for each $m = 1,\dots,r$. The size of the system (= number of degrees of freedom) is equal to the dimension of the space $S_{m,h,p}^{\tau,q}$ and it changes for $m = 1,\dots,r$. The system is solved using the Anderson acceleration method [25]. The stopping criteria and the choice of the time step are controlled in such a way that the errors arising due to the space discretization, time discretization, and iterative solution of nonlinear algebraic systems are balanced.

The meshes and polynomial degrees are chosen adaptively using a technique introduced in [26, 27]. Using a higher order reconstruction of the computed approximate solution, this technique proposes new sizes and shapes of mesh elements, as well as the corresponding polynomial degrees. The basic idea of the mesh adaptation algorithm is to minimize the number of degrees of freedom on the prescribed tolerance level for the *interpolation error* measured in the $H^1(\Omega)$-seminorm.

4. SR experiment setup

The proposed SR experiment is depicted in Fig. 2. The ring is located in the vicinity of a hillside, which is a typical application for the seepage face boundary discussed in this paper. The porous environment is anisotropic, with layers inclined into the hillside. Such experimental setup was chosen to combine the effects of a moving wetting front, seepage face boundary, and discontinuous flow domain. The domain is illustrated in the left part of Fig. 2.

The initial and boundary conditions are given as:

Γ_1 (=: Γ_N) no flow boundary

$$\frac{\partial\Psi}{\partial\vec{n}} = 0, \quad \forall(x,t)\in\Gamma_1\times t\in[0,T)$$

Γ_2 (=: Γ_D) ponding depth 5 cm

$$\Psi(x,t) = 0.05 + z, \quad \forall(x,t)\in\Gamma_2\times t\in[0,T)$$

Γ_3 (=: Γ_E) seepage face, cf. (2.7) and Section 3.4.

This is shown in the right part of Fig. 2. The origin of the coordinate system is located at the left-bottom corner of the domain.

The initial condition is a hydrostatic state with zero capillary pressure at the impermeable bottom,

$$\Psi(x,t_0) = -2\,\mathrm{m}, \quad \forall x\in\Omega. \tag{4.1}$$

The soil hydraulic properties were assumed as follows: $\alpha = 0.8\,\mathrm{m}^{-1}$, $n = 1.2$, $m = 0.167$, $\theta_s = 0.55$, $\theta_r = 0$, $S_s = 10^{-3}\,\mathrm{m}^{-1}$.

Soil properties were assumed here to be anisotropic with rotated main axes of anisotropy as depicted on Fig. 3. The rotation angle $\alpha_{xx'}$ was -30°, and so the layers were inclined into the hillslope. $K_{x'}$ was

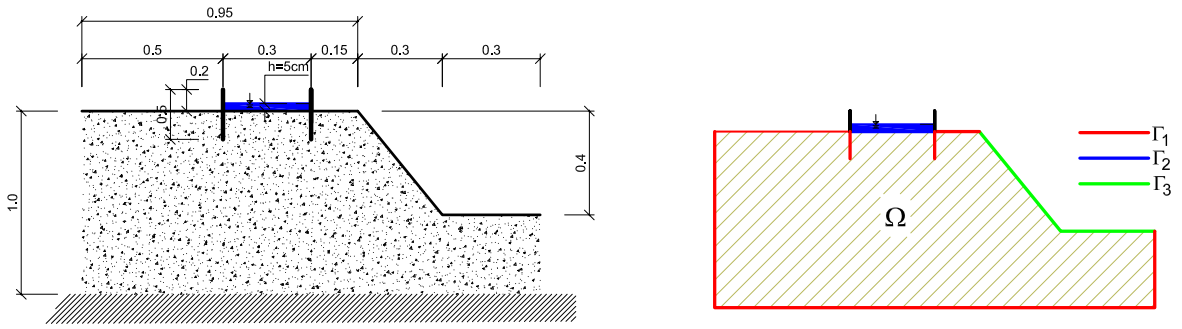

Figure 2. Scheme of the single ring infiltration experiment.

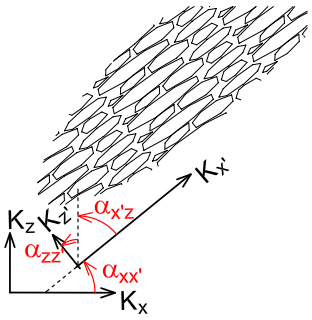

Figure 3. Example of rotated main axes of anisotropy of hydraulic conductivity, obtained from [28].

assumed to be ten times greater than $K_{z'}$. The resulting tensor of anisotropy of saturated hydraulic conductivity for our global system of coordinates was $\mathbf{K}_s = \begin{pmatrix} 1.031 \times 10^{-4} & -5.187 \times 10^{-5} \\ -5.187 \times 10^{-5} & 4.323 \times 10^{-5} \end{pmatrix} \mathrm{m.s}^{-1}$. Please note that the example presented here is purely synthetic.

4.1. Numerical results

Fig. 4 presents the approximate solution (hydraulic head) for different time levels as well as the dynamically adapted meshes. Fig. 5 shows the dynamic development of the mesh and the number of degrees of freedom. It should be noted that our case study is sensitive to discretization qualities as explained in [29]. The numerical solution exhibits physically justifiable characteristics while maitaining a low number of degrees of freedom. The maximum number of degrees of freedom was roughly 1000. Taking into account the domain size and dimension, such automatically adapted mesh is highly optimal.

Finally we also present a quantitative comparison of an adaptive computation and a computation on a fixed fine mesh. Namely, we compare the actual water flux through the input boundary

$$F(t) = -\int_{\Gamma_2} \mathbf{K}(\psi)\nabla\Psi(x,t)\cdot\boldsymbol{n}\ \mathrm{d}x \qquad (4.2)$$

and the total (accumulated flux)

$$\boldsymbol{F}(t) = -\int_0^t \int_{\Gamma_2} \mathbf{K}(\psi)\nabla\Psi(x,t')\cdot\boldsymbol{n}\ \mathrm{d}x\mathrm{d}t'. \qquad (4.3)$$

The fine mesh was chosen in such a way that both computations have roughly the same level of accuracy. Fig. 6 shows the values of the actual and total fluxes in dependence on time. We observe that the actual flux is the highest at the beginning of the computation and starting from $t \approx 0.2$ hours, it is approximately constant. Finally, when the seepage face is active, the actual flux decreases (the total flux stagnates).

Moreover, we find that both computations (adaptive and fixed meshes) give very similar behaviours. The main difference is at the end of the computation where the actual flux is already negligible. The difference is caused by a large final time step chosen by the adaptive method. Furthermore, the adaptive computation uses approximately 200 elements and 10,000 degrees of freedom. It takes 74,646 seconds. The fixed mesh computation uses 2279 elements and 45,580 degrees of freedom, and it takes 401,769 seconds. Hence, clearly, the adaptive computation is much more efficient.

References

[1] X. Xu, C. Lewis, W. Liu, et al. Analysis of single-ring infiltrometer data for soil hydraulic properties estimation: Comparison of best and wu methods. *Agricultural Water Management* **107**:34 – 41, 2012. doi:10.1016/j.agwat.2012.01.004.

[2] M. Nakhaei, J. Šimunek. Parameter estimation of soil hydraulic and thermal property functions for unsaturated porous media using the hydrus-2d code. *Journal of Hydrology and Hydromechanics* **62**(1):7–15, 2014. doi:10.2478/johh-2014-0008.

[3] L. A. Richards. Capillary conduction of liquids through porous mediums. *Journal of Applied Physics* **1**(5):318–333, 1931. doi:10.1063/1.1745010.

[4] S. C. Iden, J. R. Blöcher, E. Diamantopoulos, et al. Numerical test of the laboratory evaporation method using coupled water, vapor and heat flow modelling. *Journal of Hydrology* **570**:574 – 583, 2019. doi:10.1016/j.jhydrol.2018.12.045.

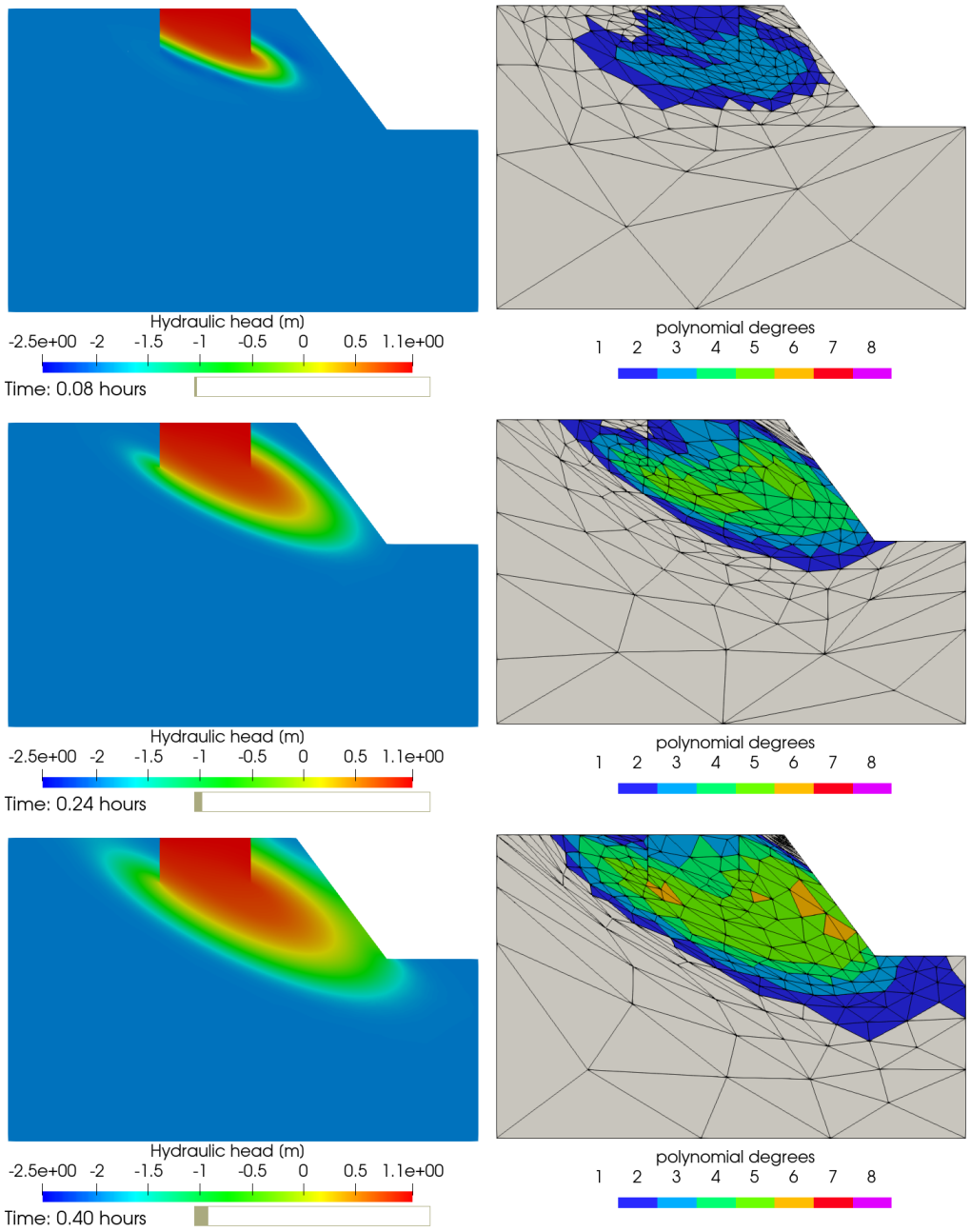

FIGURE 4. Hydraulic head and a detail of the dynamically adapted mesh.

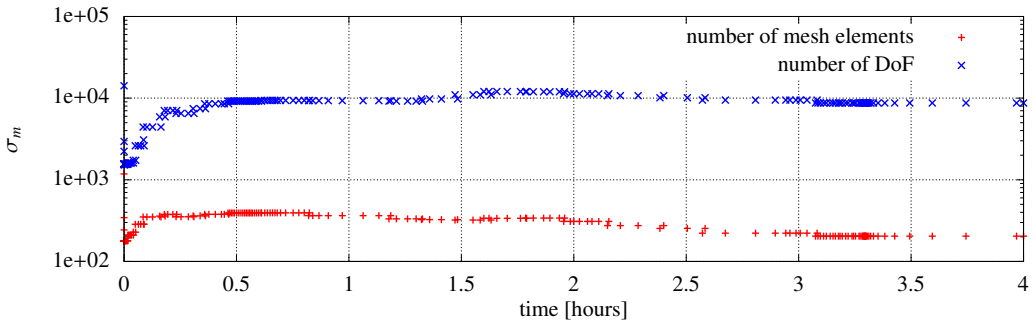

FIGURE 5. Adaptively updated mesh: number of mesh elements and number of degrees of freedom w.r.t. physical time.

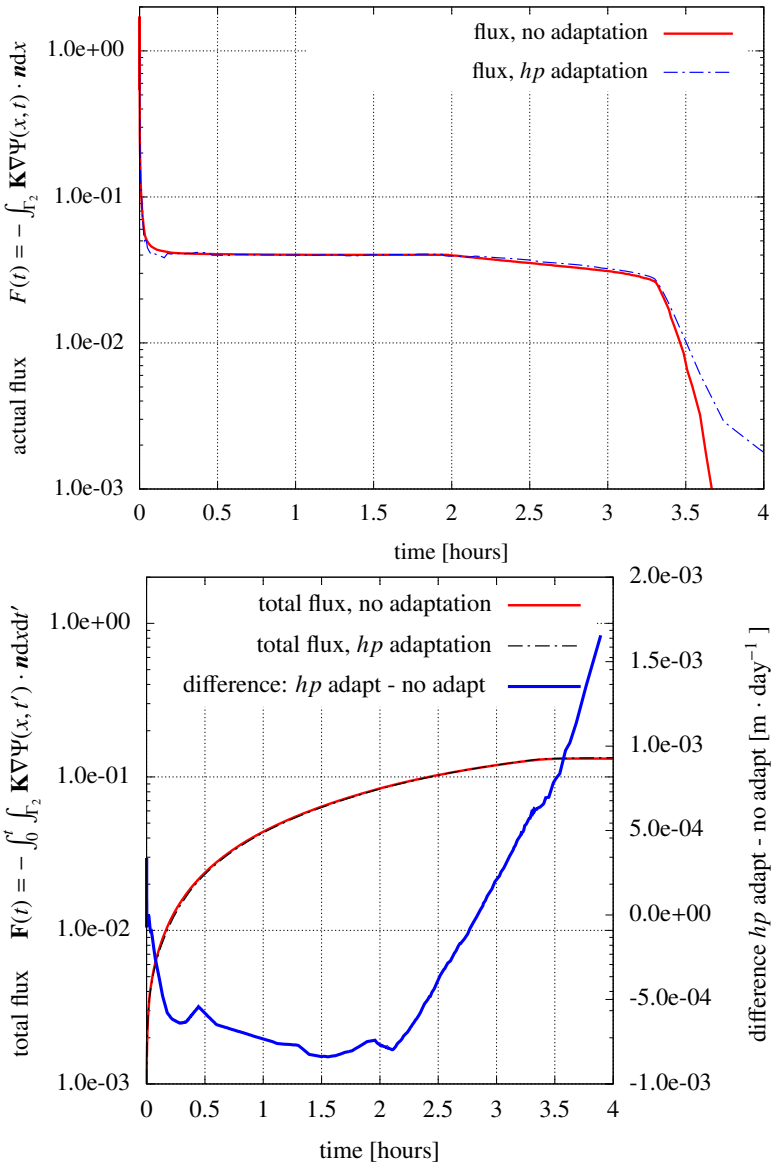

FIGURE 6. Comparison of the actual flux $F(t)$ (up) and the total (accumulated) flux (down) for the two computations, cf. (4.2)–(4.3).

[5] A. Binley, K. Beven. Vadose zone flow model uncertainty as conditioned on geophysical data. *Ground Water* **41**(2):119–127, 2003. DOI:10.1111/j.1745-6584.2003.tb02576.x.

[6] S. Würzer, N. Wever, R. Juras, et al. Modelling liquid water transport in snow under rain-on-snow conditions – considering preferential flow. *Hydrology and Earth System Sciences* **21**(3):1741–1756, 2017. DOI:10.5194/hess-21-1741-2017.

[7] M. Kuraz, P. Mayer, V. Havlicek, et al. Dual permeability variably saturated flow and contaminant transport modeling of a nuclear waste repository with capillary barrier protection. *Applied Mathematics and Computation* **219**(13):7127 – 7138, 2013. ESCO 2010 Conference in Pilsen, June 21- 25, 2010, DOI:10.1016/j.amc.2011.08.109.

[8] H. Alt, S. Luckhaus. Quasilinear elliptic-parabolic differential equations. *Mathematische Zeitschrift* **183**(3):311–341, 1983. DOI:10.1007/BF01176474.

[9] F. Otto. L^1-contraction and uniqueness for quasilinear elliptic-parabolic equations. *Journal of Differential Equations* **131**(1):20–38, 1996.

[10] F. Otto. L^1–contraction and uniqueness for unstationary saturated-unsaturated porous media flow. *Adv Math Sci Appl* **7**(2):537–553, 1997.

[11] L. Lam, D. Fredlund. Saturated-unsaturated transient finite element seepage model for geotechnical engineering. *Advances in Water Resources* **7**(3):132 – 136, 1984. DOI:10.1016/0309-1708(84)90042-3.

[12] C. Kees, M. Farthing, C. Dawson. Locally conservative, stabilized finite element methods for variably saturated flow. *Computer Methods in Applied Mechanics and Engineering* **197**(51):4610 – 4625, 2008. DOI:10.1016/j.cma.2008.06.005.

[13] J. Šembera, M. Beneš. Nonlinear Galerkin method for reaction-diffusion systems admitting invariant regions. *Journal of Computational and Applied Mathematics* **136**(1):163 – 176, 2001. DOI:10.1016/S0377-0427(00)00582-3.

[14] P. Solin, M. Kuraz. Solving the nonstationary Richards equation with adaptive hp-FEM. *Advances in Water Resources* **34**(9):1062 – 1081, 2011. New Computational Methods and Software Tools, DOI:10.1016/j.advwatres.2011.04.020.

[15] M. Tocci, C. Kelley, C. Miller. Accurate and economical solution of the pressure-head form of Richards' equation by the method of lines. *Advances in Water Resources* **20**(1):1 – 14, 1997. DOI:10.1016/S0309-1708(96)00008-5.

[16] C. Miller, C. Abhishek, M. Farthing. A spatially and temporally adaptive solution of Richards' equation. *Advances in Water Resources* **29**(4):525 – 545, 2006. DOI:10.1016/j.advwatres.2005.06.008.

[17] M. Kuraz, P. Mayer, V. Havlicek, P. Pech. Domain decomposition adaptivity for the Richards equation model. *Computing* **95**(1):501–519, 2013. DOI:10.1007/s00607-012-0279-8.

[18] M. Kuraz, P. Mayer, P. Pech. Solving the nonlinear Richards equation model with adaptive domain decomposition. *Journal of Computational and Applied Mathematics* **270**:2 – 11, 2014. Fourth International Conference on Finite Element Methods in Engineering and Sciences (FEMTEC 2013), DOI:10.1016/j.cam.2014.03.010.

[19] M. Kuraz, P. Mayer, P. Pech. Solving the nonlinear and nonstationary Richards equation with two-level adaptive domain decomposition (dd-adaptivity). *Applied Mathematics and Computation* **267**:207 – 222, 2015. The Fourth European Seminar on Computing (ESCO 2014), DOI:10.1016/j.amc.2015.03.130.

[20] V. Dolejší, M. Kuráž, P. Solin. Adaptive higher-order space-time discontinuous galerkin method for the computer simulation of variably-saturated porous media flows. *Applied Mathematical Modelling* **72**:276 – 305, 2019. DOI:10.1016/j.apm.2019.02.037.

[21] M. T. van Genuchten. Closed-form equation for predicting the hydraulic conductivity of unsaturated soils. *Soil Science Society of America Journal* **44**(5):892–898, 1980. DOI:10.2136/sssaj1980.03615995004400050002x.

[22] Y. Mualem. A new model for predicting the hydraulic conductivity of unsaturated porous media. *Water Resources Research* **12**(3):513–522, 1976. `https://agupubs.onlinelibrary.wiley.com/doi/pdf/10.1029/WR012i003p00513` DOI:10.1029/WR012i003p00513.

[23] M. Kuraz, P. Mayer, M. Leps, D. Trpkosova. An adaptive time discretization of the classical and the dual porosity model of Richards' equation. *Journal of Computational and Applied Mathematics* **233**(12):3167 – 3177, 2010. Finite Element Methods in Engineering and Science (FEMTEC 2009), DOI:10.1016/j.cam.2009.11.056.

[24] V. Dolejší, M. Feistauer. *Discontinuous Galerkin Method – Analysis and Applications to Compressible Flow*. Springer Series in Computational Mathematics 48. Springer, Cham, 2015.

[25] H. F. Walker, P. Ni. Anderson acceleration for fixed-point iterations. *SIAM J Numer Anal* **49**(4):1715–1735, 2011. DOI:10.1137/10078356X.

[26] V. Dolejší. Anisotropic *hp*-adaptive method based on interpolation error estimates in the L^q-norm. *Appl Numer Math* **82**:80–114, 2014. DOI:10.1016/j.apnum.2014.03.003.

[27] V. Dolejší. Anisotropic *hp*-adaptive method based on interpolation error estimates in the H^1-seminorm. *Appl Math* **60**(6):597–616, 2015. DOI:10.1007/s10492-015-0113-7.

[28] M. Kuraz, J. R. Bloecher. *Hydrodynamic of porous media*. CULS in Prague, 2017. Http://drutes.org/documents/notes.pdf.

[29] J. Dusek, M. Dohnal, T. Vogel. Numerical analysis of ponded infiltration experiment under different experimental conditions. *Soil and Water Research* **4**(SPECIAL ISSUE 2):22–27, 2009. DOI:10.17221/1368-SWR.